Monolayer $ThSi_2N_4$: An indirect-gap semiconductor with ultra-high carrier mobility

Cheng Lu,[1,*] Chuyan Cui,[1] Jingning Zuo,[1] Hongxia Zhong,[1,†] Shi He,[1] Wei Dai,[2] and Xin Zhong[3,‡]

[1]*School of Mathematics and Physics, China University of Geosciences (Wuhan), Wuhan 430074, China*

[2]*School of Mathematics and Physics, Jingchu University of Technology, Jingmen 448000, China*

[3]*Key Laboratory of Materials Simulation Methods & Software of Ministry of Education, College of Physics, Jilin University, Changchun 130012, China*

(Received 10 August 2023; revised 13 October 2023; accepted 9 November 2023; published 29 November 2023)

The recently synthesized $MoSi_2N_4$ monolayer [Science **369**, 670 (2020)] exhibit outstanding environmental stability, moderate band gap, and excellent mechanical properties, which opens up a new avenue for the explorations of two-dimensional (2D) MA_2Z_4 materials. Inspired by this finding, we perform comprehensive structural predictions of MSi_2N_4 monolayers with lanthanide and actinide metals at the M site. Using the CALYPSO structural search method and first-principles calculations, we identify seven MSi_2N_4 monolayers with robust ambient stabilities, four of which are metals (M = Tm, Lu, Pa, Np) and three are semiconductors (M = Ce, Th, U). Of particular interest is the $ThSi_2N_4$ monolayer, which is an indirect-gap semiconductor with ultra-high electron mobility of 14384 $cm^2\ V^{-1}\ s^{-1}$. Our results enrich the 2D MA_2Z_4 family and offer insights into the design and synthesis of novel multifunctional materials.

DOI: 10.1103/PhysRevB.108.205427

I. INTRODUCTION

Since the discovery of graphene in 2004, two-dimensional (2D) materials have continuously demonstrated their unusual physical properties and potential technical applications [1–3]. Among them, the MA_2Z_4 monolayers are an important class of 2D materials that offer selectively tailored physical properties to meet the needs of numerous applications due to the diversities of M, A, and Z components and distinct permutations [4–8]. Furthermore, the M, A, and Z components in the heptatomic layer of the MA_2Z_4 monolayer can be interchanged with different synthesis technologies, further expanding the potential for tailored properties. Currently, MA_2Z_4 monolayers are widely used in energy storage and conversion, such as supercapacitors, rechargeable batteries, and electrocatalysts. The versatility and promising properties of the MA_2Z_4 monolayers make them significant candidates for further research and development in various fields.

Recently, Hong *et al.* [4] successfully synthesized a high-quality 2D $MoSi_2N_4$ monolayer by introducing silicon to passivate nonlayered molybdenum nitride surfaces during chemical vapor deposition growth. This monolayer consists of a MoN_2 layer sandwiched between two Si-N bilayers with septuple N-Si-N-Mo-N-Si-N atomic layers, representing a typical 2D MA_2Z_4 material with excellent ambient stability. Subsequently, a series of studies on MA_2Z_4 materials have been reported, and important progresses have been made [9–14]. Theoretical calculations reveal that the MA_2Z_4 materials are different from the transition metal carbides, nitrides, and disulfides, and show more abundant and interesting characteristics due to the complexity of the structures and the diversity of components [15–17]. For instance, these characteristics include excellent mechanical properties, intriguing electronic properties [9], extensively thermal conductivities [10], pronounced optical absorptions of both visible and ultraviolet radiations [11], outstanding photocatalytic capacities [12], good spin-splitting [13], and magnetic properties [14]. Meanwhile, Cheng *et al.* [18] have declared that 2D $MoSi_2N_4$ are suitable for both the positive electrode and negative electrode materials of lithium-air batteries. A high electron mobility of about 1.4×10^4 $cm^2\ V^{-1}\ s^{-1}$ is observed in the $TiSi_2N_4$ monolayer [19]. Other potential applications including high-efficiency spintronic and valley electronic devices [13], optoelectronic devices [20], energy-saving devices based on coupling between multiple electronic degrees of freedom [21], and field-effect transistors [22] are well documented one after another. In fact, based on the particular configuration of MA_2Z_4, the researchers have devised a plethora of novel constituents and structural motifs. For example, a cadre of innovative and enduring magnetic materials have emerged, including $ScSi_2N_4$, VSi_2N_4, $MnSi_2N_4$, $FeSi_2N_4$, $CoSi_2N_4$, $NiSi_2N_4$, $CuSi_2N_4$, and $ZnSi_2N_4$ [23].

Apart from the experimental synthesis of the $MoSi_2N_4$ monolayer, Hong *et al.* [4] also conducted comprehensive density-functional theory (DFT) calculations. The calculated results verified twelve stable MA_2Z_4 monolayers with the same structure of $MoSi_2N_4$, in which the Mo atoms are replaced by the transition metals such as Ti, Zr, Nf, V, Nb, Ta, Cr, and W atoms, Si atoms are replaced by Ge atoms, and N atoms are replaced by P and As atoms, respectively. Notably, the tensile strength of the $MoSi_2N_4$ monolayer is 50.6 GPa at a critical biaxial strain of 19.5% [24]. The $MoSi_2N_4$ monolayer exhibits high lattice thermal conductivity of about

*lucheng@calypso.cn

†zhonghongxia@cug.edu.cn

‡zhongxin@calypso.cn

440 W/mK [25], mainly attributed to its large group velocities and small anharmonicity [26]. However, no lanthanide or actinide metal-based MA_2Z_4 monolayers are explored, especially for the structural and electronic properties of MA_2Z_4 monolayers under extreme conditions.

In this work, we have conducted extensive structure searches on MA_2Z_4 monolayers that contain lanthanide and actinide metals at the M site. Our goal is to identify the stable MA_2Z_4 monolayers that exhibit exceptional physical properties. The calculations indicate that the MSi_2N_4 (M = Ce, Tm, Lu, Th, Pa, U, Np) monolayers are stable at ambient conditions [27]. Electronic structure calculations reveal that the MSi_2N_4 (M = Tm, Lu, Pa, Np) monolayers exhibit metallic behavior, while the MSi_2N_4 (M = Ce, Th, U) monolayers are semiconductors. Here, we mainly focus on the three semiconductors, i.e., MSi_2N_4 (M = Ce, Th, U) monolayers. Interestingly, the $ThSi_2N_4$ monolayer shows a remarkably high carrier mobility of up to 14 384 $cm^2\ V^{-1}\ s^{-1}$, which is the highest among all the stable MA_2Z_4 monolayers.

II. COMPUTATIONAL METHODS

The structural searches on MSi_2N_4 monolayers are performed using 2D CALYPSO method in combination with first-principles calculations [28–31]. Both the fixed and variable unit cells are considered in the structural searches. We first perform the fixed unit cell of 7 atoms structural searches with stoichiometry of 1:2:4 for MSi_2N_4 (M = Ce, Th, U) monolayers, and then carry out the variable unit cells (one to four formula units) structural searches for MSi_2N_4 (M = Ce, Th, U) monolayers. For the structural relaxations and reoptimizations, we use the projector-augmented wave (PAW) potentials [32] and generalized gradient approximation (GGA) [33], as implemented in VASP code [33]. The Perdew-Burke-Ernzerhof (PBE) functionals are adopted to describe electron exchange correlations. The tested 700 eV and Monkhorst-Pack k-point grid of $15 \times 15 \times 1$ are utilized in the enthalpies and electronic structure calculations. We ensure that the total energy and force converged to be less than 10^{-6} eV and 0.001 eV/Å, respectively. A large vacuum space of 20 Å along the z axis is included to avoid spurious interactions between adjacent images. The phonon dispersion curves are calculated by using the PHONOPY package [34]. The carrier mobilities of MSi_2N_4 monolayers are calculated by the following equation [35–37]

$$\mu_{2D} = \frac{e\hbar^3 C_{2D}}{k_B T m^* m_d E_1^2}, \tag{1}$$

where C_{2D} represents the elastic moduli, T is the temperature, k_B is the Boltzmann constant, E_1 is the deformation potential constant, m^* is the effective mass, and m_d is the average effective mass of the carrier. The effective mass of m^* is calculated by fitting the parabolic function via the formula

$$\frac{1}{m^*} = \frac{1}{\hbar}\frac{\partial^2 E(k)}{\partial k^2}, \tag{2}$$

where $E(k)$ is the wavenumber k-dependent energy at the valence band maximum/conduction band minimum (VBM/CBM). The elastic modulus of a 2D monolayer is defined as [38]

$$C_{2D} = \frac{\frac{\partial^2 E}{\partial(\Delta l/l_0)^2}}{S_0}, \tag{3}$$

where E is the total energy, and S_0 is the cell area at equilibrium.

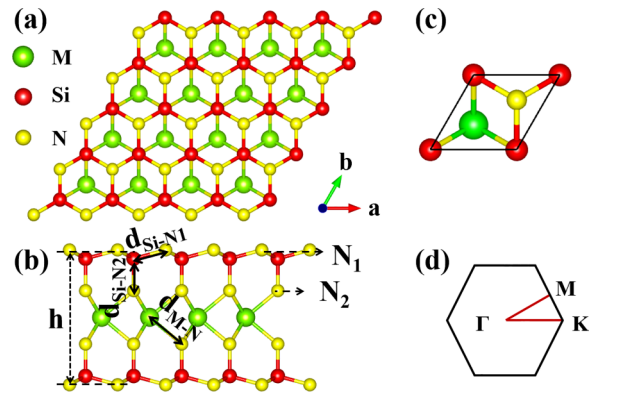

FIG. 1. The geometrical structures of MSi_2N_4 (M = Ce, Th, U) monolayers. (a) Top view and (b) side view. h is the layer thickness. The bonds of Si-N (d_{Si-N1}, d_{Si-N2}) and M-N (d_{M-N}) in MSi_2N_4 (M = Ce, Th, U) monolayers are marked by the black double arrow. (c) The unit cell of MSi_2N_4 (M = Ce, Th, U) monolayers. (d) The Brillouin zone of MSi_2N_4 (M = Ce, Th, U) monolayers.

III. RESULTS AND DISCUSSION

A. Crystal structure and stability

Figure 1 shows the ground-state structures of 2D MSi_2N_4 (M = Ce, Th, U) monolayers in a $3 \times 3 \times 1$ supercell. These monolayers belong to the hexagonal lattice with space group $P6m2$ symmetry, which is the same as the synthesized $MoSi_2N_4$ monolayer [4]. Each MSi_2N_4 monolayer is composed of septuple atomic layers arranged as N-Si-N-M-N-Si-N. The local structure of the middle MN_2 layer is similar to that of 2H-MoS_2, which is sandwiched by two Si-N bilayers. Three Si atoms and three N atoms form a folding chair hexatomic ring, and M atoms are coordinated by six Si atoms and occupy the center of the trigonal prisms. The SiN layers are connected to the MN_2 layers by vertically aligned N-Si chemical bonds. The optimized structural parameters are displayed in Table I. The lattice constant of the $CeSi_2N_4$ monolayer is 3.041 Å, which is obviously smaller than that of the $ThSi_2N_4$ monolayer (3.159 Å). However, the atomic radius of Ce (1.85 Å) is similar to that of Th (1.80 Å). This abnormal

TABLE I. The calculated lattice constant (a), layer thickness (h), bond lengths of Si-N (d_{Si-N1}, d_{Si-N2}) and M-N (d_{M-N}), and band gaps of MSi_2N_4 (M = Ce, Th, U) monolayers.

Monolayer	a (Å)	h (Å)	d_{Si-N1} (Å)	d_{Si-N2} (Å)	d_{M-N} (Å)	E_g (eV)	E_{g_HSE} (eV)
$CeSi_2N_4$	3.041	7.226	1.814	1.733	2.259	0.49	1.81
$ThSi_2N_4$	3.159	7.350	1.880	1.753	2.339	0.42	1.48
USi_2N_4	3.031	7.410	1.815	1.754	2.284	0.13	1.27

TABLE II. The calculated effective mass m^* (m_e), elastic modulus C_{2D} (N/m), DP constant E_1 (eV), and carrier mobility μ ($cm^2\ V^{-1}\ s^{-1}$) for the electrons and holes of MSi_2N_4 (M = Ce, Th, U) monolayers at 300 K. The corresponding values of InSe [40], BP [41], $MoSi_2N_4$, and MoS_2 [4] monolayers are also listed for comparison.

monolayers	carrier type	m_x^* (m_e)	m_y^* (m_e)	C_{2D_X} (N/m)	C_{2D_Y} (N/m)	E_{1X} (eV)	E_{1Y} (eV)	μ_{2D_X} ($cm^2\ V^{-1}\ s^{-1}$)	μ_{2D_Y} ($cm^2\ V^{-1}\ s^{-1}$)
$CeSi_2N_4$[a]	electron	0.872	0.872	339.31	343.10	1.69	1.41	3347.90	4825.93
	hole	2.958	2.957	339.31	343.10	3.05	3.26	88.82	78.64
$ThSi_2N_4$[a]	electron	0.418	0.418	273.21	293.82	1.64	1.58	12 474.56	14 383.81
	hole	3.346	3.346	273.21	293.82	1.86	1.92	151.09	151.26
USi_2N_4[a]	electron	3.630	6.467	335.78	379.57	4.49	4.07	20.24	15.63
	hole	2.289	1.331	335.78	379.57	4.36	3.74	94.32	248.93
InSe [40]	electron	0.180	0.190	45.99	46.10	4.27	3.97	1619.51	1779.16
	hole	2.140	2.020	45.99	46.10	1.28	1.89	134.90	65.70
BP [41]	electron	0.170	1.240	21.50	91.43	0.71	4.20	11 361.29	191.52
	hole	0.160	7.640	21.50	91.43	2.74	1.92	341.30	62.63
BP[b]	electron	0.179	1.270	21.48	91.43	0.63	4.13	13 530.84	188.89
	hole	0.177	11.15	21.48	91.43	2.81	1.65	234.24	45.91
$MoSi_2N_4$ [4]	electron	0.486	0.486	530.44	531.13	11.04	10.54	261.96	287.79
	hole	0.683	0.683	530.44	531.13	3.69	3.69	1226.87	1188.85
$MoSi_2N_4$[b]	electron	0.452	0.416	479.82	480.79	9.92	9.92	356.65	388.30
	hole	0.669	0.669	479.82	480.79	3.34	3.65	1093.80	1148.30
MoS_2 [4]	electron	0.460	0.480	127.44	128.16	10.88	11.36	72.16	60.32
	hole	0.570	0.600	127.44	128.16	5.29	5.77	200.52	152.18

[a]This work. The results are calculated by DFT + U method.
[b]This work. The results are calculated by standardized DFT method.

behavior may be attributed to the fact that the $4f$ electrons of lanthanide atoms are tightly bounded to the nucleus, and the d and s electrons become the free electrons. As a result, the Ce atom can use more electrons to participate in the chemical bonding. The difference in chemical bonding leads to variations in bond distances, resulting in a smaller bond length d_{M-N} of the $CeSi_2N_4$ (2.259 Å) monolayer compared to the $ThSi_2N_4$ (2.339 Å) monolayer.

The atomic radii of actinide atoms follow a similar trend to the main group elements, decreasing with increasing atomic number. Specifically, the atomic radius of U is smaller than that of Th. As expected, the lattice constant and bond length d_{M-Si} of USi_2N_4 monolayer are smaller than those of $ThSi_2N_4$ monolayer. Interestingly, the Si-N bond lengths remain largely unchanged in the sandwiched MA_2Z_4 monolayers (M = Ce, Th, U) compared to $MoSi_2N_4$ monolayer, indicating minimal impact from atom substitutions on the upper and lower layers. In contrast, the M-Si bonds in the monolayers display noticeable changes. To confirm the stabilities of the $CeSi_2N_4$, USi_2N_4, and $ThSi_2N_4$ monolayers, we have calculated the phonon dispersions, as shown in Figs. 2(a)–2(c). The phonon dispersions are calculated by using the density-functional-perturbation theory (DFPT). A $6 \times 6 \times 1$ Monkhorst-Pack grid is used. No imaginary frequencies are observed in the Brillouin zone, indicating the MSi_2N_4 (M = Ce, Th, U) monolayers are dynamically stable. To determine the thermal stabilities of MSi_2N_4 (M = Th, Ce, U) monolayers, we have performed *ab initio* molecular dynamics simulations. A $4 \times 4 \times 1$ supercell is used in the *ab initio* molecular dynamics (AIMD) calculations for 10 ps with a time interval of 3 fs. As shown in Fig. S1 [27], it can be seen that the structures remain stable at a temperature of 300 K after molecular dynamics (MD) simulations of 10 ps.

Generally, a complex folded structure exhibits a higher elastic modulus than a flat structure for a 2D monolayer. By parabolic fitting the deformation degree and the energy of structure after deformation, the elastic modulus of MSi_2N_4 (M = Ce, Th, U) monolayers are obtained and listed in Table II. All the elastic constants are satisfied with the mechanical stability criteria [39], indicating the mechanical stabilities of MSi_2N_4 (M = Ce, Th, U) monolayers. Interestingly, the MSi_2N_4 (M = Ce, Th, U) monolayers exhibit exceptional in-plane stiffness due to their hybridized bond networks. For example, the C_{2D} of $ThSi_2N_4$ monolayer is 294 N/m, which is one order higher than that of InSe [40] and black phosphorus (BP) [41]. The Young's modulus and shear modulus of $CeSi_2N_4$ monolayer are the highest among the MSi_2N_4 (M = Ce, Th, U) monolayers, which is consistent with the C_{2D} values. The high elastic modulus indicates the robust capacity to suppress lattice vibrations and resist deformations, thus reducing the number of phonons and the probabilities of electrons being scattered by phonons. Although the C_{2D} of $ThSi_2N_4$ calculated by GGA + U method is the smallest among the MSi_2N_4 (M = Ce, Th, U) monolayers, its value is still larger than that of the common 2D layered materials [41].

B. Electronic structures

The electronic band structures of MSi_2N_4 (M = Ce, Th, U) monolayers are calculated by PBE and HSE06 functionals. The results are presented in Fig. S2 [27]. The PBE results show that $ThSi_2N_4$ monolayer exhibits a 0.42 eV indirect band gap. The conduction band minimum (CBM) of $ThSi_2N_4$ monolayer locates at Γ point. The valence band maximum (VBM) of $ThSi_2N_4$ monolayer locates between M−Γ.

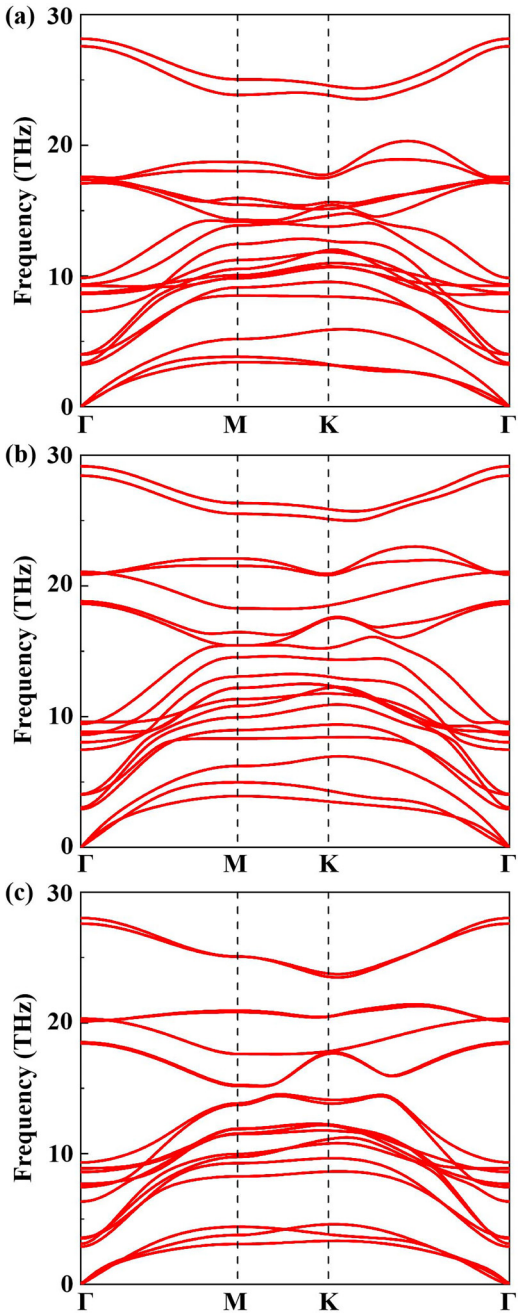

FIG. 2. The phonon dispersions of MSi_2N_4 (M = Th, Ce, U) monolayers. (a) $ThSi_2N_4$, (b) $CeSi_2N_4$, and (c) USi_2N_4.

Normally, the PBE functional is usually underestimated in the band gap. Thus, we further calculate the band structures of $ThSi_2N_4$ monolayer through HSE method. Compared to PBE level, the HSE results show a larger band gap of 1.48 eV for $ThSi_2N_4$ monolayer, however the band dispersions are almost unchanged. Similar results are also observed in $MoSi_2N_4$ monolayer [4]. More details about the band edge constituents are obtained through the projected density of states (PDOS). Obviously, the valence band edge of $ThSi_2N_4$ monolayer is mainly contributed by the p state of N atom, while the conduction band edge is dominated by the f and d states of Th atom. Moreover, the partial charge-density isosurfaces for VBM and CBM of $ThSi_2N_4$ monolayer are also calculated

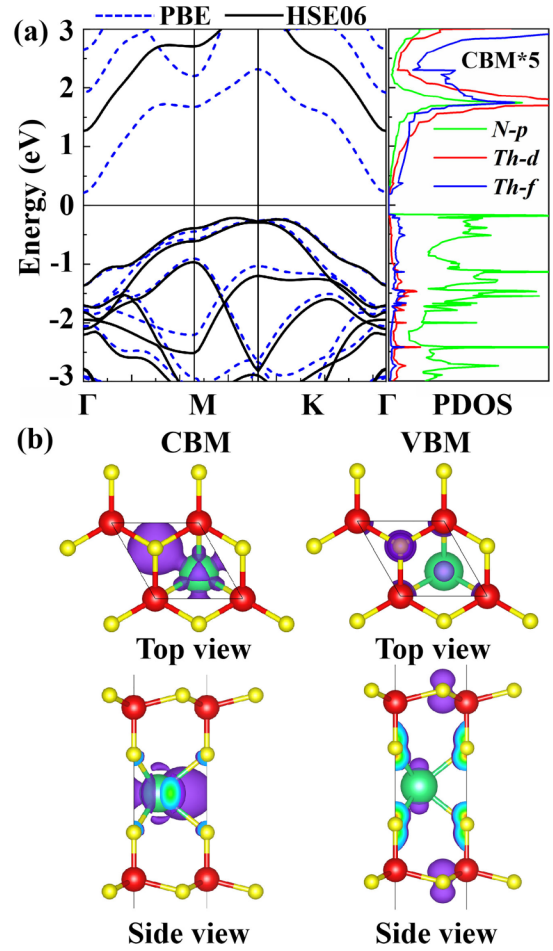

FIG. 3. (a) The electronic band structures and (b) partial charge density isosurfaces for CBM and VBM of $ThSi_2N_4$ monolayers. The solid black lines and the dotted blue lines represent the band structures calculated by HSE06 and PBE methods, respectively. The isosurface value is 0.7 e/Bohr^3.

and depicted in Fig. 3(b). In considering the strongly electronic interactions of lanthanides and actinides, we have also used the DFT + U method to calculate the electronic band structures, as shown in Fig. S3 [27]. Based on the linear response approach method [42], we have tested the Hubbard U parameters, which are 4.99 eV, 2.59 eV, and 2.36 eV for MSi_2N_4 (M = Ce, Th, U) monolayers. In addition, it is also important to consider spin-orbit coupling (SOC) interactions for transition metals. From the spin-orbit coupling calculations, as shown in Fig. S4 [27], it is observed that the changes of the energy bands of USi_2N_4 monolayer are obvious. The spin-up and spin-down energy bands intersect the Fermi level, indicating the magnetism of USi_2N_4 monolayer. To verify the magnetism, we have conducted the calculations within a $2 \times 2 \times 1$ supercell and determined the local magnetic moments of USi_2N_4 monolayer. The local magnetic moments of U atoms in USi_2N_4 monolayer are approximately 1.6 μ_B. By contrast, the DFT + U calculations indicate that both $ThSi_2N_4$ and $CeSi_2N_4$ monolayers are nonmagnetic (NM).

The spatial contributions of atomic orbitals to the band edges in $ThSi_2N_4$ monolayer are different from those in $MoSi_2N_4$ and MoS_2 monolayers, where both valence and

conduction band edges are primarily dominated by the d orbitals of the Mo atom [43]. The electronic band structures of $CeSi_2N_4$ and USi_2N_4 monolayers are also calculated. The results are shown in Fig. S2 [27], respectively. In $CeSi_2N_4$ monolayer, the CBM is located at Γ point and is mainly contributed from the f electrons of Ce, its VBM locates between M−K and is also mainly contributed from p electrons of N. As for USi_2N_4 monolayer, the CBM is located at K, while the VBM is located between Γ−M. In contrast to $CeSi_2N_4$ and $ThSi_2N_4$ monolayers, the valence electrons of USi_2N_4 monolayer near the Fermi level are mainly contributed by the f electrons of U. The band gaps of MSi_2N_4 (M = Ce, Th, U) monolayers significantly decreases compared to $MoSi_2N_4$ monolayer, which is attributed to the substitutions of M atoms that contribute more electrons near the Fermi level.

C. Carrier mobility

The flexible 2D semiconductors with high carrier mobility are promising for high-speed nanoelectronics. However, contemporary 2D semiconductors, especially monolayer semiconductors, have limited carrier mobility at ambient conditions. Typically, the charge carrier mobilities of contemporary 2D semiconductors, such as transition metal dichalcogenides and InSe, are in the range of $10^0 - 10^3$ cm^2 V^{-1} s^{-1}. Specifically, the charge carrier mobilities of these materials at ambient temperature are all below 2000 cm^2 V^{-1} s^{-1}. The recently synthesized $MoSi_2N_4$ monolayer shows notable hole and electron mobilities of 1200 and 280 cm^2 V^{-1} s^{-1}, respectively, which are 4 to 6 times larger than those of MoS_2 monolayer (∼200 cm^2 V^{-1} s^{-1}). The carrier mobility is closely related to the lattice scattering. Thus, it is reasonable to speculate that the MA_2Z_4 monolayers may also exhibit the high mobility as $MoSi_2N_4$ monolayer [44–52].

We then estimate the acoustic-phonon-limited carrier mobilities of MSi_2N_4 (M = Ce, Th, U) monolayers by the deformation potential theory [38]. To confirm the reliability of the calculated method, we first calculate the carrier mobilities of 2D BP and $MoSi_2N_4$ monolayer. The calculated carrier mobilities of 2D black phosphorus and $MoSi_2N_4$ monolayer are 13 531 cm^2 V^{-1} s^{-1} and 1094 cm^2 V^{-1} s^{-1}, respectively. These values are in good agreement with previous results of ∼11 361 cm^2 V^{-1} s^{-1} [41] and ∼1200 cm^2 V^{-1} s^{-1} [4], verifying the reliabilities of the current calculations. The effective mass and carrier mobility of MSi_2N_4 (M = Ce, Th, U) monolayers are calculated at ambient temperature. In fact, to achieve high carrier mobility in 2D monolayers, three criteria should be satisfied: (i) the small effective mass m^*, (ii) the small deformation potential constant E_1, and (iii) the larger elastic modulus C_{2D}. Remarkably, the 2D $ThSi_2N_4$ monolayer satisfies the above three criteria for achieving high carrier mobility. The carrier mobility of $ThSi_2N_4$ monolayer is ultra-high, reaching values of 16 957 cm^2 V^{-1} s^{-1} with standardized DFT calculations (See Table S1 [27]). Normally, the Hubbard U parameters can change the electronic structures, and thus affect the elastic properties and the carrier mobilities of MSi_2N_4 (M = Ce, Th, U) monolayers. We further extend the calculations of the carrier mobilities with DFT + U method. The calculated results are listed in Table II. It can be seen from Table II that the carrier mobility of $ThSi_2N_4$ is 14 384 cm^2 V^{-1} s^{-1} with DFT + U method, which is obviously larger than those of InSe (∼1779 cm^2 V^{-1} s^{-1}) [40] and MoS_2 (∼200 cm^2 V^{-1} s^{-1}) [4]. Therefore, in the following, we mainly focus on the 2D $ThSi_2N_4$ monolayer to explore the underlying mechanisms of its ultra-high carrier mobility.

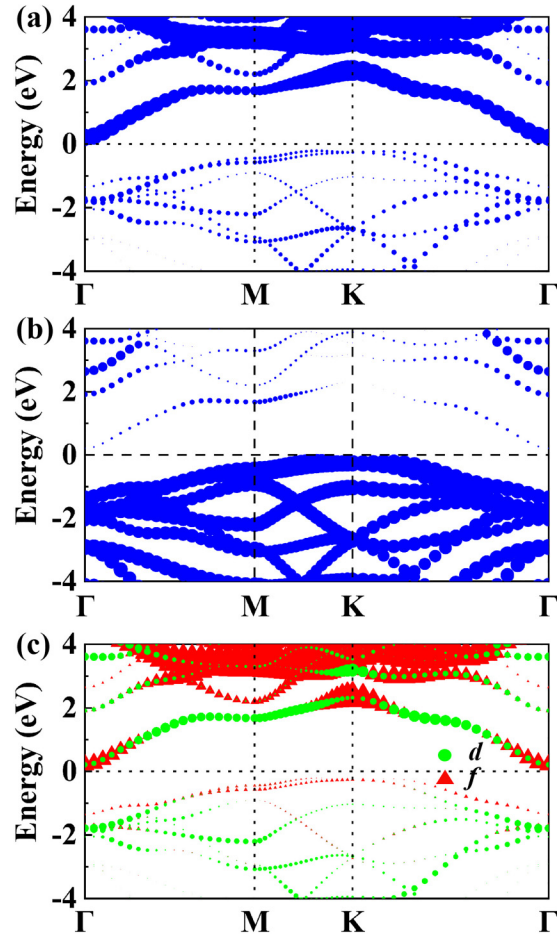

FIG. 4. (a) The projection bands of Th atom. (b) The projection bands of N atom and (c) the fractional projection bands of Th atom.

The effective masses of electrons and holes in $ThSi_2N_4$ monolayer are 0.418 m_e and 3.346 m_e, respectively. The calculated electron effective mass is comparable to those of $MoSi_2N_4$ ($m^*_{\text{electron}} = 0.486\ m_e$) [4] and MoS_2 ($m^*_{\text{electron}-x} = 0.480\ m_e$, $m^*_{\text{electron}-y} = 0.480\ m_e$) [4] monolayers. It can be seen from Fig. 3 that the conduction band dispersions of $ThSi_2N_4$ monolayer are sharp along Γ−M and Γ−K directions. The dispersive bands cause the larger second derivative of $\partial^2 E(k)/\partial k^2$, which hence leads to the small effective mass. To explore the underlying mechanisms, we calculate the projected band structures of $ThSi_2N_4$ monolayer, as shown in Fig. 4. Our results reveal that the main contributor of the conduction band of $ThSi_2N_4$ monolayer is Th atom, while the N atom mainly contributes to the valence band. Furthermore, the orbital-resolved band structures demonstrate the CBM of $ThSi_2N_4$ monolayer is primarily dominated by the f electrons of Th atom. Thus, the small effective mass observed in the $ThSi_2N_4$ monolayer can be attributed to the presence of actinide Th atom. This phenomenon indicates a weak coupling between the carriers (both electrons and holes) and the

lattice, enabling efficient carrier transport within the crystal and resulting in high carrier mobility.

The deformation potential constant E_1 is determined by fitting CBM and VBM with respect to the strains. The electron deformation potential constant E_1 of $ThSi_2N_4$ monolayer is 1.64/1.58 eV, which is one order of magnitude lower than that of $MoSi_2N_4$ (11.04/10.54 eV) monolayer. The CBM charge distributions of $ThSi_2N_4$ monolayer show small electron clouds, indicating the less electron transfer between the adjacent atoms. Consequently, the overlap degree of the wave functions is low, and $ThSi_2N_4$ monolayer is insensitive to the applied strains, which causes the small deformation potential constant E_1. The small value of E_1 leads to a small residual energy of the carrier after phonon scattering, which is conducive to carrier transport. Therefore, the small deformation potential constant E_1 is one of the factors contributing to the high carrier mobility of $ThSi_2N_4$ monolayer.

The ultra-high carrier mobility of 14 384 $cm^2\ V^{-1}\ s^{-1}$ in $ThSi_2N_4$ monolayer is attributed to its small effective mass. The carrier mobility of $ThSi_2N_4$ is larger than other high mobility 2D semiconductors such as InSe ($\sim$1779 $cm^2\ V^{-1}\ s^{-1}$), and BP($\sim$11361 $cm^2\ V^{-1}\ s^{-1}$). By contrast, USi_2N_4 monolayer is hole dominated with a much lower carrier mobility of 249 $cm^2\ V^{-1}\ s^{-1}$. The carrier mobilities of MSi_2N_4 (M = Ce, Th) monolayers are higher than those of $MoSi_2N_4$ ($\sim$1226 $cm^2\ V^{-1}\ s^{-1}$), and MoS_2 ($\sim$200 $cm^2\ V^{-1}\ s^{-1}$) monolayers. The $CeSi_2N_4$ and $ThSi_2N_4$ monolayers improve carrier mobility compared with the previously synthesized $MoSi_2N_4$ monolayer with the similar configuration. The electron and hole carrier mobilities of MSi_2N_4 (M = Ce, Th, U) monolayers are different, which indicates that the MSi_2N_4 monolayers possess both excellent carrier mobility and substantial carrier polarization.

D. Absorption spectra and strain effect

Carrier polarization is useful in a variety of practical applications, such as photocatalytic carrier separation. The calculated band gaps of MSi_2N_4 (M = Ce, Th, U) monolayers also suggest the potential visible-light absorption properties of MSi_2N_4 monolayers. The light absorption coefficients of MSi_2N_4 (M = Ce, Th, U) monolayers are calculated and shown in Fig. 5. Notably, the absorption spectra of MSi_2N_4 (M = Ce, Th, U) monolayers are found to exhibit the main absorption peaks in the visible-light range. The maximum peak of $ThSi_2N_4$ monolayer occurs at the photon energy of 2.4 eV with the light absorption rate of approximately 10%. The main peak of $ThSi_2N_4$ monolayer appears in the green light region of visible light. $CeSi_2N_4$ and USi_2N_4 monolayers also exhibit $\sim$10% and $\sim$13% absorptivity in the visible region. It is noteworthy that the visible-light absorptivity of the MSi_2N_4 (M = Ce, Th, U) monolayers is found to be higher than that of BP ($\sim$7%) [53]. In addition, the USi_2N_4 monolayer displays small peaks in both infrared and ultraviolet regions. To explore the influence of excitonic effects in absorbance of $ThSi_2N_4$ monolayer, we have used the *ab initio GW* approximation plus Bethe-Salpeter equation (GW_0-BSE) method, which is one of the most common and accurate methods [54–56]. In order to achieve the numerical accuracy in GW_0, the empty bands are chosen to be 10 times greater than the

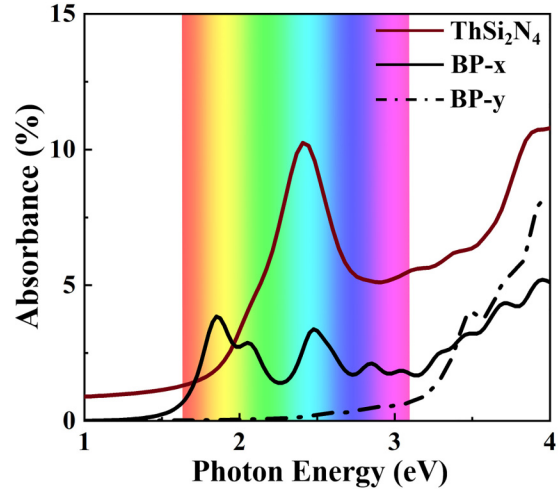

FIG. 5. The optical absorption spectra of $ThSi_2N_4$ and BP monolayer. The visible-light energy range is marked in color.

number of occupied bands. Meanwhile, the BSE is solved by a fine grid of 15 × 15 × 1. The optical absorption spectra calculated by GW_0-BSE method are shown in Fig. S5 [27]. The results show that the light absorption spectra in both x and y directions are coincident for MSi_2N_4 (M = Ce, Th, U) monolayers, indicating their isotropic behaviors to polarized light. The maximum peak in the visible-light range of $ThSi_2N_4$ monolayer occurs at the photon energy of 2.84 eV with the light absorption rate of about 10%. The main peak of $ThSi_2N_4$ monolayer is shifted from the green light region to the blue light region of the visible light.

We then study the strain effect on MSi_2N_4 (M = Ce, Th, U) monolayers. Interestingly, the MSi_2N_4 (M = Ce, Th, U) monolayers undergo the semiconductor to metal transition under different strains. The valence band (VB) and conduction band (CB) are deformed under different structural

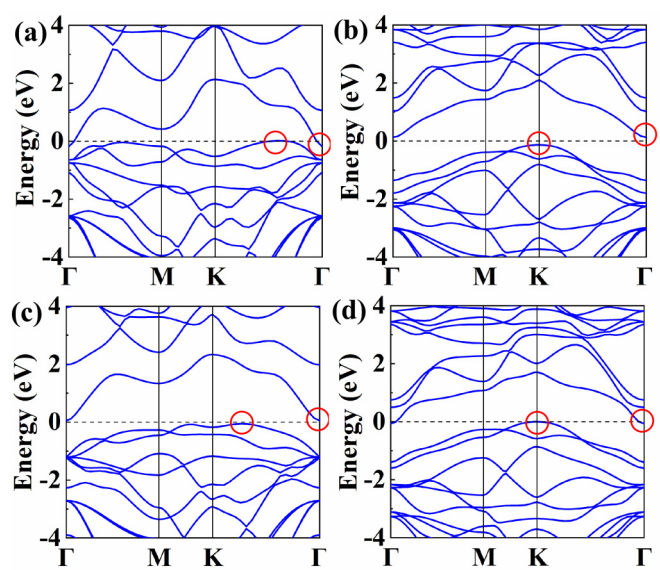

FIG. 6. The band structures of $ThSi_2N_4$ monolayer under biaxial strains. (a) Compressed 10%, (b) compressed 5%, (c) stretch 5%, (d) stretch 10%.

deformations. The change of band structure mainly reflects in the squeezing and transformation of the highest VB and the lowest CB near the Fermi level, while the energy changes of CBM and VBM are small. The semiconductor to metal transition of $ThSi_2N_4$ monolayer occurs at 10% compression and 10% tension, and the VBM position changes and shifts to K point under tensile deformation, as shown in Fig. 6. Compared to $ThSi_2N_4$ monolayer, the $CeSi_2N_4$ monolayer is more obstinate, and the transition from semiconductor to metal of $CeSi_2N_4$ monolayer is difficult, requiring at least 20% compression or 13% tension. Specifically, the VBM of $CeSi_2N_4$ monolayer moves from Γ point to M point with compressed strain of 10% under compressive deformation, and the band gap changes simultaneously from indirect to direct. The USi_2N_4 monolayer shows an indirect band-gap semiconductor under compressive strain up to 10% and transforms to metal at 13% compression and 5% tension. The results are presented in Figs. S6 and S7 [27], which show the abundant electronic modulate behaviors of MSi_2N_4 (M = Ce, Th, U) monolayers.

IV. CONCLUSION

In summary, we carry out extensive structure searches of MSi_2N_4 monolayers with lanthanide and actinide metals at the M site by 2D CALYPSO structural prediction method and first-principles calculations. We uncover three semiconducting MSi_2N_4 (M = Ce, Th, U) monolayers with robust stabilities at ambient conditions. The $ThSi_2N_4$ monolayer is an indirect-gap semiconductor showing abundant electronic modulate behaviors. The electron mobility of $ThSi_2N_4$ monolayer is 14 384 $cm^2\ V^{-1}\ s^{-1}$, which is higher than those of the conventional 2D monolayers, such as MoS_2, InSe, and BP. The current study identifies new members of the 2D MA_2Z_4 family and describes their structural and electronic properties, which provide significant insights into the design and synthesis of advanced functional materials.

ACKNOWLEDGMENTS

This work is supported by National Natural Science Foundation of China (Grants No. 522881024, No. 12174352, No. 520900244, No. 12374009, and No. 12104421) and the Fundamental Research Funds for the Central Universities, China University of Geosciences (Wuhan) (Grant No. G1323523065).

[1] A. H. C. Neto, N. M. R. Peres, K. S. Novoselov, A. K. Geim, and F. Guinea, The electronic properties of graphene, Rev. Mod. Phys. **81**, 109 (2009).

[2] C. Lee, X. Wei, J. W. Kysar, and J. Hone, Measurement of the elastic properties and intrinsic strength of monolayer graphene, Science **321**, 385 (2008).

[3] M. Liu, X. Yin, E. Ulin-Avila, B. Geng, T. Zentgraf, L. Ju, F. Wang, and X. Zhang, A graphene-based broadband optical modulator, Nature (London) **474**, 64 (2011).

[4] Y. L. Hong, Z. Liu, L. Wang, T. Zhou, W. Ma, C. Xu, S. Feng, L. Chen, M. L. Chen, D. M. Sun *et al.*, Chemical vapor deposition of layered two-dimensional $MoSi_2N_4$ materials, Science **369**, 670 (2020).

[5] Y. J. Deng, Y. J. Yu, M. Z. Shi, Z. X. Guo, Z. H. Xu, J. Wang, X. H. Chen, and Y. B. Zhang, Quantum anomalous Hall effect in intrinsic magnetic topological insulator $MnBi_2Te_4$, Science **367**, 895 (2020).

[6] A. Y. Gao, Y. F. Liu, C. W. Hu, J. X. Qiu, C. Tzschaschel, B. Ghosh, S. C. Ho, D. Bérubé, R. Chen, H. Sun *et al.*, Layer Hall effect in a 2D topological axion antiferromagnet, Nature (London) **595**, 521 (2021).

[7] M. M. Otrokov, I. I. Klimovskikh, H. Bentmann, D. Estyunin, A. Zeugner, Z. S. Aliev, S. Gaß, A. U. B. Wolter, A. V. Koroleva, A. M. Shikin *et al.*, Prediction and observation of an antiferromagnetic topological insulator, Nature (London) **576**, 416 (2019).

[8] R. Islam, B. Ghosh, C. Autieri, S. Chowdhury, A. Bansil, A. Agarwal, and B. Singh, Tunable spin polarization and electronic structure of bottom-up synthesized $MoSi_2N_4$ materials, Phys. Rev. B **104**, L201112 (2021).

[9] A. Priydarshi, Y. S. Chauhan, S. Bhowmick, and A. Agarwal, Large and anisotropic carrier mobility in monolayers of the MA_2Z_4 series (M = Cr, Mo, W; A = Si, Ge; and Z = N, P), Nanoscale **14**, 11988 (2022).

[10] C. L. Zhang, F. Wei, X. H. Zhang, W. Chen, C. C. Chen, J. B. Hao, and B. N. Jia, Thermoelectric properties of monolayer $MoSi_2N_4$ and $MoGe_2N_4$ with large seebeck coefficient and high carrier mobility: A first principles study, J. Solid State Chem. **315**, 123447 (2022).

[11] Y. L. Wang and Y. Ding, A stable low-symmetry T-phase of MSi_2Z_4 (M = Mo, W; Z = P, As) nanosheets with promising electronic and photovoltaic properties: Insight from first-principles calculations, Appl. Phys. Lett. **121**, 073101 (2022).

[12] C. Lin, X. Feng, D. Legut, X. P. Liu, Z. W. Seh, R. F. Zhang, and Q. F. Zhang, Discovery of efficient visible-light driven oxygen evolution photocatalysts: Automated high-throughput computational screening of MA_2Z_4, Adv. Funct. Mater. **32**, 2207415 (2022).

[13] S. Sheoran, S. Monga, A. Phutela, and S. Bhattacharya, Coupled spin-valley, Rashba effect and hidden persistent spin polarization in WSi_2N_4 family, J. Phys. Chem. Lett. **14**, 1494 (2023).

[14] J. S. Zhang, Y. Wang, C. Q. Hua, S. B. Yang, Y. J. Liu, J. M. Luo, T. F. Liu, J. Nai, and X. Y. Tao, Prediction of bipolar VSi_2As_4 and VGe_2As_4 monolayers with high Curie temperature and strong magnetocrystalline anisotropy, Phys. Rev. B **106**, 235401 (2022).

[15] Y. Yin, Q. H. Gong, M. Yi, and W. L. Guo, Emerging versatile two-dimensional $MoSi_2N_4$ family, Adv. Funct. Mater. **33**, 2214050 (2023).

[16] C. H. Li and L. Cheng, Intrinsic electron transport in monolayer $MoSi_2N_4$ and WSi_2N_4, J. Appl. Phys. **132**, 075111 (2022).

[17] M. Kong, S. Murakami, and T. Zhang, A comprehensive study of complex non-adiabatic exciton dynamics in $MoSi_2N_4$, Mat. Today Phys. **27**, 100814 (2022).

[18] L. R. Cheng, Z. Z. Lin, X. M. Li, and X. Chen, 2D $MoSi_2N_4$ as electrode material of Li-air battery - a DFT study, J. Nanopart. Res. **25**, 55 (2023).

[19] K. Ren, H. B. Shu, K. Wang, and H. S. Qin, Two-dimensional MX_2Y_4 systems: Ultrahigh carrier transport and excellent hydrogen evolution reaction performances, Phys. Chem. Chem. Phys. **25**, 4519 (2023).

[20] G. G. Liu, Z. H. Xu, L. Huang, X. B. Xiao, and T. Chen, Bandgap engineering and optoelectronic properties of 2D WSi_2N_4 nanosheets: a first principle calculations, Physica E **146**, 115530 (2023).

[21] L. Liang, Y. Yang, X. H. Wang, and X. Li, Tunable valley and spin splittings in VSi_2N_4 bilayer, Nano Lett. **23**, 858 (2023).

[22] Y. Shu, Y. Q. Liu, Z. Cui, R. Xiong, Y. G. Zhang, C. Xu, J. Y. Zheng, C. L. Wen, B. Wu, and B. Sa, Efficient ohmic contact in monolayer CrX_2N_4 (X = C, Si) based field-effect transistors, Adv. Electron. Mater. **9**, 2201056 (2023).

[23] Z. X. Zhao, X. H. Duan, X. T. Fang, X. C. Wang, and W. B. Mi, Prediction of electronic structure and magnetic anisotropy of two-dimensional MSi_2N_4 (M = 3*d* transition-metal) monolayers, Appl. Surf. Sci. **611**, 155693 (2023).

[24] Q. F. Li, W. X. Zhou, X. G. Wan, and J. Zhou, Strain effects on monolayer $MoSi_2N_4$: Ideal strength and failure mechanism, Physica E **131**, 114753 (2021).

[25] B. Mortazavi, B. Javvaji, F. Shojaei, T. Rabczuk, A. V. Shapeev, and X. Y. Zhuang, Exceptional piezoelectricity, high thermal conductivity and stiffness and promising photocatalysis in two-dimensional $MoSi_2N_4$ family confirmed by first-principles, Nano Energy **82**, 105716 (2021).

[26] J. H. Yu, J. Zhou, X. G. Wan, and Q. F. Li, High intrinsic lattice thermal conductivity in monolayer $MoSi_2N_4$, New J. Phys. **23**, 033005 (2021).

[27] See Supplemental Material at http://link.aps.org/supplemental/10.1103/PhysRevB.108.205427 for mechanical and electronic properties of MSi_2N_4 (M = Th, Ce, U) monolayers.

[28] Y. Wang, J. Lv, L. Zhu, and Y. Ma, Crystal structure prediction via particle-swarm optimization, Phys. Rev. B **82**, 094116 (2010).

[29] Y. Wang, J. Lv, L. Zhu, and Y. Ma, CALYPSO: A method for crystal structure prediction, Comput. Phys. Commun. **183**, 2063 (2012).

[30] W. G. Sun, B. Chen, X. F. Li, F. Peng, A. Hermann, and C. Lu, Ternary Na-PH superconductor under high pressure, Phys. Rev. B **107**, 214511 (2023).

[31] Q. Z. Duan, J. Y. Shen, X. Zhong, H. Y. Lu, and C. Lu, Structural phase transition and superconductivity of ytterbium under high pressure, Phys. Rev. B **105**, 214503 (2022).

[32] P. E. Blöchl, Projector augmented-wave method, Phys. Rev. B **50**, 17953 (1994).

[33] G. Kresse and J. Furthmuller, Efficient iterative schemes for ab initio total-energy calculations using a plane-wave basis set, Phys. Rev. B **54**, 11169 (1996).

[34] A. Togo, F. Oba, and I. Tanaka, First-principles calculations of the ferroelastic transition between rutile-type and $CaCl_2$-type SiO_2 at high pressures, Phys. Rev. B **78**, 134106 (2008).

[35] J. S. Qiao, X. H. Kong, Z. X. Hu, F. Yang, and W. Ji, High-mobility transport anisotropy and linear dichroism in few-layer black phosphorus, Nat. Commun. **5**, 4475 (2014).

[36] J. Y. Xi, M. Q. Long, L. Tang, D. Wang, and Z. G. Shuai, First-principles prediction of charge mobility in carbon and organic nanomaterials, Nanoscale **4**, 4348 (2012).

[37] S. Takagi, A. Toriumi, M. Iwase, and H. Tango, On the universality of inversion layer mobility in Si MOSFET's: Part II-effects of surface orientation, IEEE Trans. Electron Devices **41**, 2357 (1994).

[38] J. Bardeen and W. Shockley, Deformation potentials and mobilities in non-polar crystals, Phys. Rev. **80**, 72 (1950).

[39] F. Mouhat and F. X. Coudert, Necessary and sufficient elastic stability conditions in various crystal systems, Phys. Rev. B **90**, 224104 (2014).

[40] Y. He, M. Zhang, J. J. Shi, Y. L. Cen, and M. Wu, Improvement of visible-light photocatalytic efficiency in a novel $InSe/Zr_2CO_2$ heterostructure for overall water splitting, J. Phys. Chem. C **123**, 12781 (2019).

[41] Y. Song, J. B. Pan, Y. F. Zhang, H. T. Yang, and S. X. Du, Monolayer iridium sulfide halides with high mobility transport anisotropy and highly efficient light harvesting, J. Phys. Chem. Lett. **12**, 6007 (2021).

[42] M. Cococcioni and S. de Gironcoli, Linear response approach to the calculation of the effective interaction parameters in the LDA+U method, Phys. Rev. B **71**, 035105 (2005).

[43] X. Hong, J. Kim, S. Shi, Y. Zhang, C. Jin, Y. Sun, S. Tongay, J. Wu, Y. Zhang, and F. Wang, Ultrafast charge transfer in atomically thin MoS_2/WS_2 heterostructures, Nat. Nanotechnol. **9**, 682 (2014).

[44] J. Shi, B. L. Jiang, C. Li, F. Y. Yan, D. Wang, and J. J. Wan, Review of transition metal nitrides and transition metal nitrides/carbon nanocomposites for supercapacitor electrodes, Mater. Chem. Phys. **245**, 122533 (2020).

[45] R. S. Ningthoujam and N. S. Gajbhiye, Synthesis, electron transport properties of transition metal nitrides and applications, Prog. Mater. Sci. **70**, 50 (2015).

[46] X. H. Liu, H. Zhang, Z. X. Yang, Z. H. Zhang, X. Fan, and H. Liu, Structure and electronic properties of $MoSi_2P_4$ monolayer, Phys. Lett. A **420**, 127751 (2021).

[47] J. Y. Wang, R. Q. Zhao, Z. F. Liu, and Z. R. Liu, Widely tunable carrier mobility of boron nitride-embedded graphene, Small **9**, 1373 (2013).

[48] L. Cheng, C. M. Zhang, and Y. Y. Liu, Intrinsic charge carrier mobility of 2D semiconductors, Comput. Mater. Sci. **194**, 110468 (2021).

[49] J. Du, C. X. Xia, Y. M. Liu, X. P. Li, Y. T. Peng, and S. Y. Wei, Electronic characteristics of *p*-type transparent SnO monolayer with high carrier mobility, Appl. Surf. Sci. **401**, 114 (2017).

[50] S. Calnan and A. N. Tiwari, High mobility transparent conducting oxides for thin film solar cells, Thin Solid Films **518**, 1839 (2010).

[51] W. Li, S. Ponce, and F. Giustino, Dimensional crossover in the carrier mobility of two dimensional semiconductors: the case of InSe, Nano Lett. **19**, 1774 (2019).

[52] L. Cheng, C. Zhang, and Y. Liu, The optimal electronic structure for high-mobility 2D semiconductors: Exceptionally high hole mobility in 2D antimony, J. Am. Chem. Soc. **141**, 16296 (2019).

[53] H. J. Monkhorst and J. D. Pack, Special points for Brillouin-zone integrations, Phys. Rev. B **13**, 5188 (1976).

[54] D. Y. Qiu, F. H. da Jornada, and S. G. Louie, Screening and many-body effects in two-dimensional crystals: Monolayer MoS_2, Phys. Rev. B **93**, 235435 (2016).

[55] H. Katow, R. Akashi, Y. Miyamoto, and S. Tsuneyuki, First-principles study of the optical dipole trap for two-dimensional excitons in graphane, Phys. Rev. Lett. **129**, 047401 (2022).

[56] B. Ram and H. Mizuseki, Tetrahexcarbon: A two-dimensional allotrope of carbon, Carbon **137**, 266 (2018).